

## Supplementary Information - “Ultrasound reforms drops”

Lokesh Malik,<sup>1</sup> Subhas Nandy,<sup>1</sup> Niladri Sekhar Satpathi,<sup>1</sup>  
Debasish Ghosh,<sup>1</sup> Thomas Laurell,<sup>2</sup> and Ashis Kumar Sen<sup>1,\*</sup>

<sup>1</sup>*Micro Nano Bio Fluidics Unit, Department of Mechanical Engineering,  
Indian Institute of Technology (IIT) Madras, Chennai, Tamil Nadu, India*

<sup>2</sup>*Division of Nanobiotechnology, Department of Biomedical Engineering, Lund University, Lund, Sweden*

(Dated: July 26, 2024)

---

### This PDF file includes:

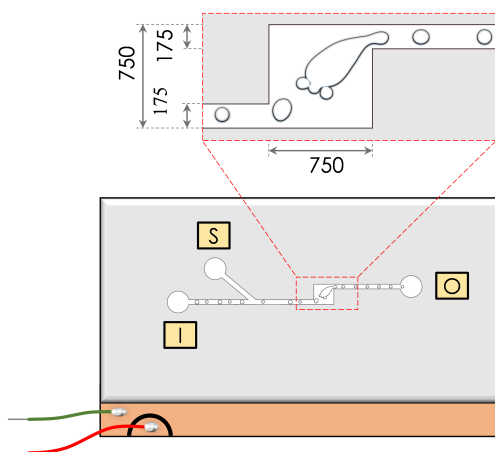
Supplementary Text (Sections: 1 to 9)  
Figs. S1 to S9  
Movies S1 to S7  
References (1 to 7)

---

**Sections:** The supplementary text is spread across the following 9 sections.

1. Schematic of microfluidic chip
2. Particle focussing experiments
3. Trapping characteristics of a drop
4. Variation of splitted drop characteristics with varying acoustic power and continuous medium flow rate
5. Theoretical model - scaling of acoustic energy
6. Acoustic streaming and acousto-coalescence induced micromixing
7. High-throughput operation
8. Improved response time
9. Positioning of the transducer element with respect to the chamber

Supplementary Movies - Legends



---

**Fig. S1: Schematic of microfluidic chip.** Schematic of the microfluidic device showing the channel design (through the glass), PZT transducer bonded to the bottom of the silicon, and electrical connections. I, S, and O are used to indicate inlet, spacer, and outlet channels. A zoomed-in view of the acoustic chamber is shown indicating the dimensions of the inlet/ outlet channel and the chamber.

---

\* [ashis@iitm.ac.in](mailto:ashis@iitm.ac.in)

## 1. SCHEMATIC OF MICROFLUIDIC CHIP

The schematic of the microfluidic device and the dimensions are shown through Fig. S1.

## 2. PARTICLE FOCUSSED EXPERIMENTS

We perform stop-flow particle focussing experiments to determine the resonating frequency and to locate the pressure nodal region. By varying frequency in steps within the range 0.8 to 1.1 MHz, we record the time of focussing of particles towards the pressure nodal region at different frequencies. The frequency at which the focussing time is the least is taken to be the resonating frequency, which is found as 0.875 MHz. Also, the final positions of the particles indicate the pressure nodal region which is found to be aligned with one of the diagonals of the square chamber, also confirmed by simulation results indicated by the region where the normalized first order acoustic pressure magnitude,  $|p_1^*|$  is minimum as seen in Fig. S2. At the resonating frequency, the magnitude of the pressure amplitude attains a maximum value which is found to be  $\sim \mathcal{O}(1)$  MPa, calculated numerically.

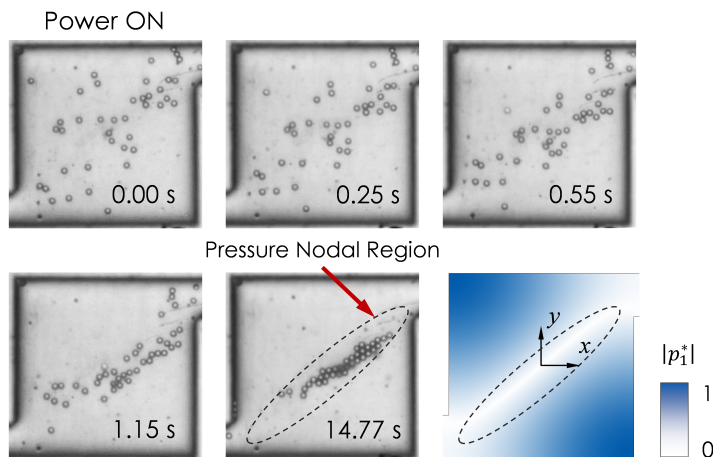


**Fig. S2:** Particle focussing experiments and acoustic pressure variation. Time series of micrographs of stop-flow particle focussing experiments are shown for  $25\mu\text{m}$  particles suspended in mineral oil actuated at a voltage of 8V. Numerically calculated, normalized acoustic first order pressure magnitude ( $|p_1^*|$ ) variation is also shown.

## 3. TRAPPING CHARACTERISTICS OF A DROP

Individual drops (within the Rayleigh limit) behave similar to particles [1] in regard to the trapping characteristics. The ratio of acoustic trapping energy scale,  $E_A = E_{ac}k\phi D_i^4 \sim V_{pp}^2 k\phi D_i^4$  and the viscous energy scale,  $W_V \sim \eta U D_i^2$  is defined as a dimensionless energy parameter  $\beta = V_{pp}^2 k\phi D_i^2 / (\eta U)$ , where  $E_{ac}, V_{pp}, k, \phi$  ( $= (1 - \kappa_d/\kappa_c)/3 + (\rho_d - \rho_c)/(\rho_c + 2\rho_d)$ ) [2],  $D_i, \eta$ , and  $U (= Q_c/W_i/h)$  are the acoustic energy density, peak-to-peak actuation voltage, acoustic wave number ( $= 2\pi/\lambda$ ), acoustic contrast factor, average incoming drop size, viscosity of the continuous phase fluid, and average velocity of the continuous phase fluid through the inlet/outlet channel, respectively with  $\lambda$  being the wavelength of the acoustic wave inside the chamber,  $\kappa$  being the compressibility (d for discrete particle/ drop and c for continuous fluid medium) and  $\rho$  being the density. As done in our previous study [1], when normalized with the kinetic energy of the incoming drop, the two energy scales:  $E_A^*$  and  $W_V^*$  are used for demarcating the trapping and non-trapping regimes as shown in Fig. S3. The trapping and non-trapping (shaded) regimes are demarcated with a solid line with slope,  $\beta = \beta_{cr} = 1.50$ . Trapping and non-trapping of drops occurs for cases with  $\beta > \beta_{cr}$  and  $\beta \leq \beta_{cr}$ , respectively.

## 4. VARIATION OF SPLITTED DROP CHARACTERISTICS WITH VARYING ACOUSTIC POWER AND CONTINUOUS MEDIUM FLOW RATE.

Transport of splitted drop for a range of actuation voltage and continuous medium flow rate, is presented via time snaps of micrographs and a plot, shown in Fig. S4. The size of the splitted drop decreases with the increase in both, actuation voltage and continuous medium flow rate.

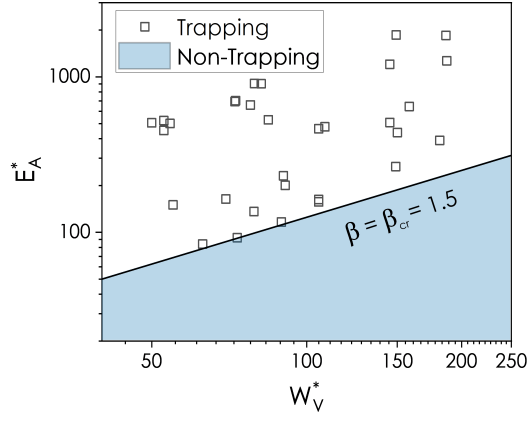


**Fig. S3:** Regime plot for trapping and non-trapping cases of drops subjected to bulk acoustic waves flowing through the acoustic chamber.  $E_A^*$  and  $W_V^*$  are the acoustic trapping energy and viscous energy scales, normalized with the kinetic energy of the incoming drop at the instant when it enters the chamber.

### 5. THEORETICAL MODEL - SCALING OF ACOUSTIC ENERGY

Since acoustic radiation force is a volumetric force, we define the acoustic energy scale,  $E^a$  directly by considering the pressure  $P$  exerted by the sound wave on the phase separating boundary (interface) and the volume  $V (\sim \pi D^3)$  of the drop, as  $E^a = PV$ . Here,  $P \sim 2E_{ac}(1 + Z^2 - 2Zn)/(1 + Z)^2$ , where  $E_{ac}$  is the time averaged energy density in the continuous phase,  $Z$  is the ratio of acoustic impedance of continuous phase to discrete phase given by  $\rho_c c_c / (\rho_d c_d)$ , and  $n$  is the ratio of speed of sound in continuous to discrete phase given by  $c_c / c_d$ . The expression for pressure [3], strictly valid for a case of normal incidence of the sound wave over on a plane interface, is used here as an approximation providing a scale that represents the momentum lost by the sound wave in the direction perpendicular to the interface per unit time per unit area of the interface. The energy density scaled as  $V_{pp}^2$  [4] is a representative scale which is approximated for the present case of two-dimensional acoustic cavity although it does not incorporate the effect of position dependent acoustic energy density across the cavity. Hence, the scale

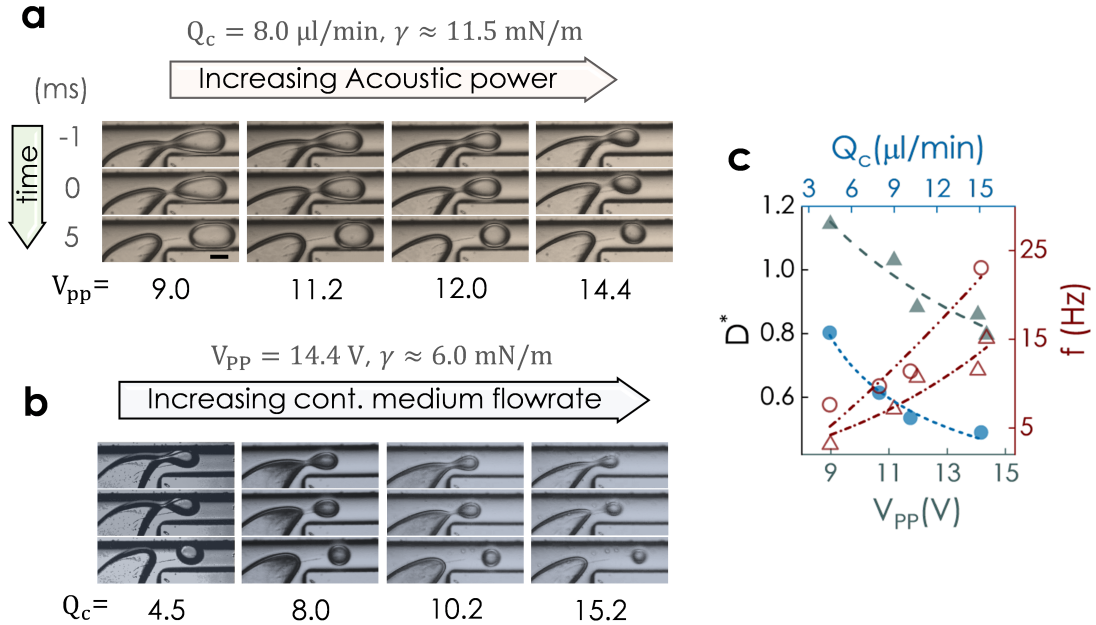


**Fig. S4:** Variation of splitted drop characteristics. Transport of splitted drop shown, at three different time instants where time = 0 corresponds to the splitting instant; for variation in actuation voltage in (a); and for variation in continuous medium flow rate in (b). (c) Effect of varying  $V_{pp}$  and  $Q_c$  on dimensionless drop size,  $D^*$ . Filled circle and triangle represent size variation with flow rate and actuation voltage, respectively. Hollow circle and triangle represent frequency variation with flow rate and actuation voltage, respectively. Scale bar measures  $100 \mu\text{m}$ .

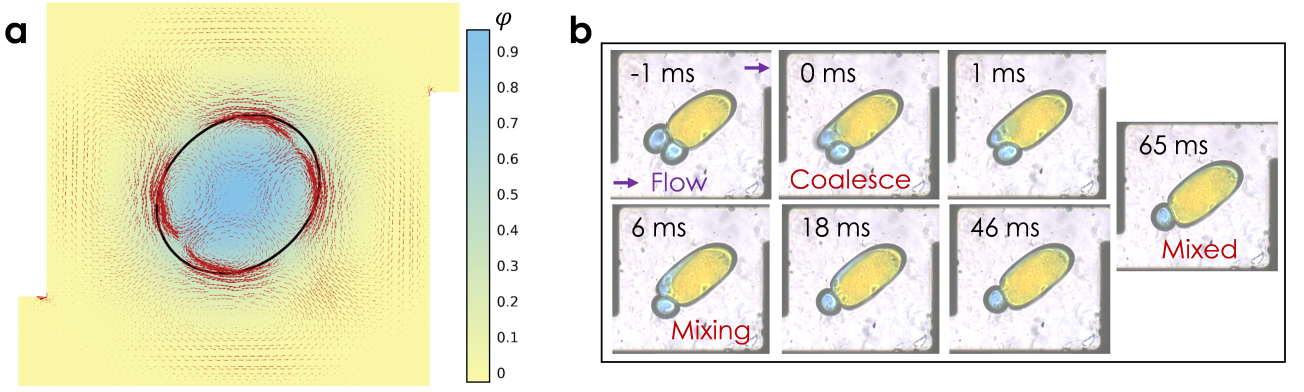


**Fig. S5: Acoustic streaming and acousto-coalescence induced micromixing.** (a) Acoustic streaming velocity inside the chamber is shown via a arrow (length of the arrows indicate the velocity magnitude) map over a color map of the volume fraction,  $\varphi$  of discrete to the continuous phase fluid. (b) Time series of experimental micrographs showing coalescence of drop and its mixing with the trapped plug.

for acoustic energy becomes,  $E^a \sim 2\pi D^3 V_{pp}^2 (1 + Z^2 - 2Zn)/(1 + Z)^2$ .

## 6. ACOUSTIC STREAMING AND ACOUSTO-COALESCENCE INDUCED MICROMIXING.

We show the details of acoustic streaming and acousto-coalescence induced micromixing through Fig. S5: Fig. S5a for acoustic streaming velocity and Fig. S5b for time-snaps of mixing between the droplet and the plug. Acoustic streaming velocity shown via arrow map in Fig. S5a, is numerically obtained using the simulation scheme given below:

We study the steady-state acoustic streaming inside the chamber by using the perturbation approach and solving the first (variables indicated by subscript, 1) and second-order (variables indicated by subscript, 2) field equations sequentially, taking into account both the dispersed as well as the continuous phase. In particular, the first-order field equations are solved in the two phases independently, taking into account the continuity of normal velocity and normal stresses at the interface. The time-averaged quantities involving the products of the first-order field variables act as acoustic source terms for the second-order effects observed within the acoustofluidic chamber system. The second-order continuity and momentum equations for the bulk of the two fluids can then be written as,

$$\begin{aligned} \rho_{0,j} \nabla \cdot \langle \vec{V}_{2,j} \rangle &= - \langle \rho_{1,j} \vec{V}_{1,j} \rangle \\ -\nabla p_{2,j} + \mu_{0,j} \nabla^2 \langle \vec{V}_{2,j} \rangle &= \langle i\omega \rho_{1,j} \vec{V}_{1,j} \rangle + \rho_{0,j} \langle (\vec{V}_{1,j} \cdot \nabla) \vec{V}_{1,j} \rangle \end{aligned}$$

Here, the subscript  $j = 1, 2$  refers to the dispersed phase (plug) and the continuous phase (background fluid medium), respectively,  $p_2$  is the second-order acoustic pressure,  $\vec{V}_1$  is the first-order acoustic velocity and  $\vec{V}_2$  is the second-order acoustic velocity. According to the proposed numerical method in the literature [5], the right-hand side term of the first equation (written above) is added as a mass source term into the Laminar flow module, while the right-hand side term of the second equation (written above) is implemented as a body force in the Laminar flow module, individually in the two phases. The interfacial tension at the fluid-fluid interface is accounted for by including the Surface Tension force in the momentum equation using the Two-Phase Flow, Level Set module. We aim at simulating the acoustic streaming velocity distribution within the bulk of the individual phases by imposing a slip-velocity condition at the fluid-fluid interface as highlighted in the literature [6] and given below,

$$\begin{aligned} u_L &= \frac{-1}{4\omega} \text{Re} \left\{ u_1 \frac{\partial u_1^*}{\partial x} + v_1 \frac{\partial u_1^*}{\partial y} + u_1^* \left[ (2+i) \left( \frac{\partial u_1}{\partial x} + \frac{\partial v_1}{\partial y} \right) \right] \right\} \\ v_L &= \frac{-1}{4\omega} \text{Re} \left\{ u_1 \frac{\partial v_1^*}{\partial x} + v_1 \frac{\partial v_1^*}{\partial y} + v_1^* \left[ (2+i) \left( \frac{\partial u_1}{\partial x} + \frac{\partial v_1}{\partial y} \right) \right] \right\} \end{aligned}$$

Considering the time-scale of development of acoustic streaming to be relatively much smaller as compared to the time scale of our experimental observations, the temporal terms are eliminated from the equations. The acoustic streaming velocity distribution in the two phases are obtained by solving the Laminar Fluid Flow and Two-Phase Flow, Level Set modules simultaneously using a stationary formulation.

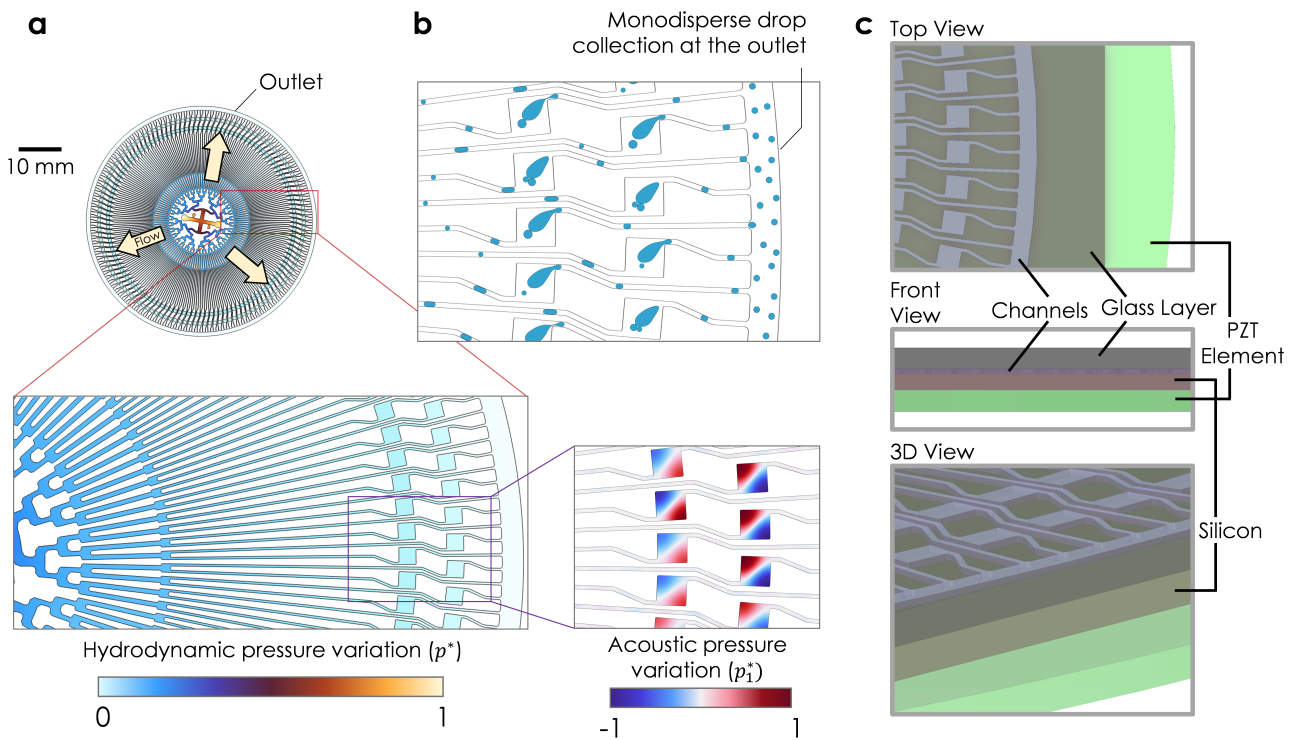


**Fig. S6: A parallelized high-throughput drop production unit.** (a) A computer-aided design of the microfluidic chip. Radially outwards arrows indicate the flow direction from inlet at the center to the outlet at the periphery. Zoomed-in views show the normalized hydrodynamic pressure variation ( $p^*$ ) and the normalized acoustic pressure distribution ( $p_1^*$ ) modelled in the device using numerical simulations (flow simulation and acoustic full device simulation [7], respectively). The later shows the simultaneous presence of the acoustic pressure nodal regions (PNR) across all the chambers, which forms the basis of possibility of a large-scale parallel drop generating platform. This high throughput design aims at producing drops together via 256 identical acoustic chambers employed in parallel at an overall drop generation frequency greater than 5 kHz from a microfluidic chip of size about 5 cm in diameter. (b) Schematic of the parallelized monodisperse drop generation through acoustic chambers and collection through a common outlet. (c) Top, front and 3-D view of the geometry considered for 3-D acoustic full device simulation [7] which models the coupled multi-physics: pressure acoustics, solid mechanics and electrostatics.

## 7. HIGH THROUGHPUT OPERATION

We show the details of the high throughput operation of our setup in Fig. S6 via introduction of a parallel drop production unit enabling multiple identical acoustofluidics devices in parallel.

## 8. IMPROVED RESPONSE TIME

We conduct control experiments to record the response time of a conventional droplet generator via the hydrodynamic control as compared to the response time of our setup via the acoustic control. For this purpose, a conventional droplet generator is connected to the upstream of the acoustic chamber, and the setup is operated both without and with acoustics, sequentially. The setup is operated first, without actuating acoustics. For this purpose, we set the discrete and the continuous medium fluids at fixed flow rates and observe the generation of droplets from the conventional droplet generator, upstream of the chamber. As the droplet arrive in the chamber and achieve an equilibrium size, we record the size of the droplets. We further repeat this process for a set of values of the flow rate combinations, by keeping the discrete flow as fixed and varying the continuous medium flow rate in steps for a range of values, and simultaneously record the equilibrium droplet size and the time taken by the system to hydrodynamically respond to the change in the flow rate, for each flow rate condition, in terms of achieving the new equilibrium droplet size. Secondly, we use acoustics to control the droplet size instead of controlling it hydrodynamically. For this, we operate at fixed hydrodynamical conditions and actuate acoustics when conventionally generated droplets arrive in the chamber. We observe trapping, coalescing and splitting of droplets through the phenomena as explained in detail in the manuscript. We record the resulting size of the reformed droplets in the re-constructed emulsion and also the time taken by the system to acoustically respond to the external actuation in terms of reforming the droplets. As expected, the results show that the acoustic

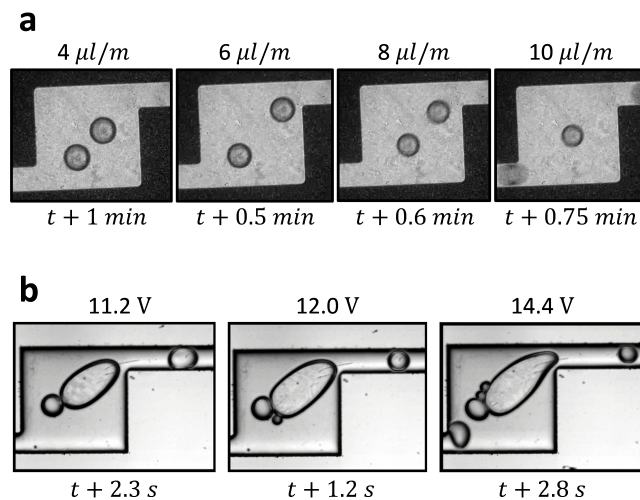


**Fig. S7: Response time study of hydrodynamic system compared to acoustic setup.** (a) Time snaps of different experiments showing the droplets generated through a conventional droplet generator at various flow rate values and the time required ( $\sim \text{min}$ ) for the hydrodynamic system to (respond) attain new equilibrium droplet size after changing the hydrodynamic condition at time,  $t$ . (b) Time snaps of different experiments showing the droplets generated through our acoustic chamber setup at various actuation voltage conditions and the time required ( $\sim \text{sec}$ ) for the acoustic system to (respond) reform the droplets after actuating acoustics at time,  $t$ .

response ( $\sim \text{sec}$ ) is far quicker as compared to the slow hydrodynamic response ( $\sim \text{min}$ ), as shown in Fig. S7.

## 9. POSITIONING OF THE TRANSDUCER ELEMENT WITH RESPECT TO THE CHAMBER

Here, we test our platform for various configurations in terms of the position of the PZT transducer element with respect to the chamber. We achieve this through 3D simulations by shifting the transducer in a linear (Fig. S8) and an angular (Fig. S9) fashion, with respect to the position of the chamber. We find that these shifts in the PZT transducer element, do not disturb the formation of pressure nodal region across the diagonal of the chamber, with the resulting acoustic pressure amplitude being comparable across all the configurations, of the order  $\sim 10^5 \text{ Pa}$ , as shown in the scale color bars (Unit -  $\text{Pa}$ ). The methodology adopted for simulations is similar [7] to the one already described through Fig. S6. All the configurations shown in Fig. S8 and S9 have the exactly same input variables, most importantly the actuation voltage ( $V_{pp} = 11 \text{ V}$ ) and the acoustic wave frequency ( $f_r \pm 0.8\% f_r$ , where  $f_r$  is the resonating frequency). Thus, the fact that all the configurations invariably show the acoustic pressure amplitude of the same order and exhibit the diagonal pressure nodal region at similar resonating frequencies, indicates that there is negligible effect of the orientation of the transducer element with respect

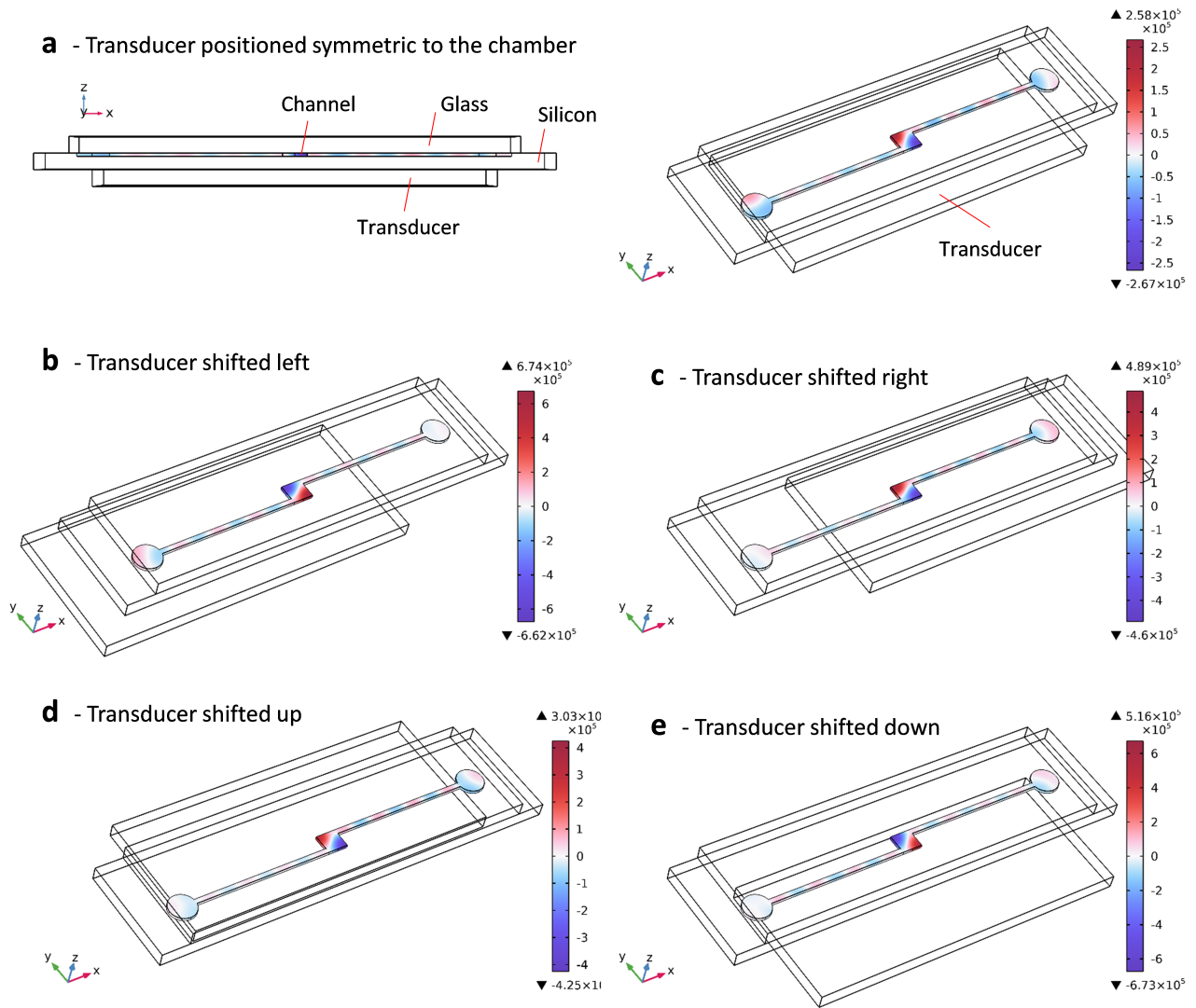


**Fig. S8:** Linear shifts (3 mm along  $x$  direction: b - left, c - right and 1.5 mm along  $y$  direction: d - up, e - down) in the position of PZT transducer element with respect to the chamber, compared to the case (a - symmetric) with no offset.

to the chamber, on the reported phenomena.

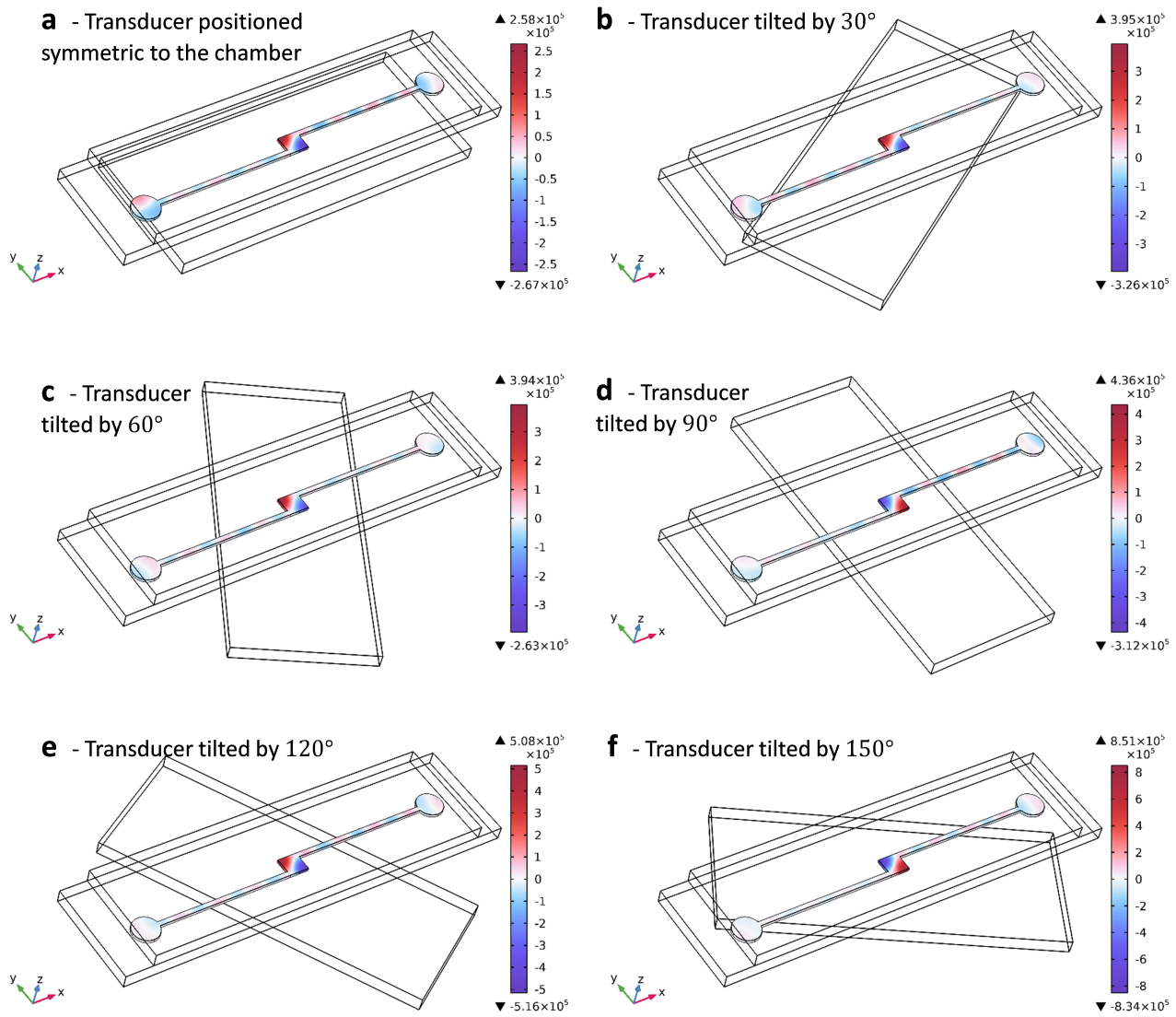


**Fig. S9:** Angular shifts (along  $x - y$  plane: b -  $30^\circ$ , c -  $60^\circ$ , d -  $90^\circ$ , e -  $120^\circ$ , f -  $150^\circ$ ) in the position of PZT transducer element with respect to the chamber, compared to the case (a -  $0^\circ$ ) with no tilt. The angle is measured from the  $x$  axis.

### SUPPLEMENTARY MOVIES - LEGENDS

**Movie S1:** Continuous nozzle-less drop generation phenomenon. The video shows a zoomed view of the splitting zone. Playback speed is 3.5x slower than realtime.

**Movie S2:** Trapping, coalescence and splitting mechanisms. The video shows the overall phenomenon with a focus on the key mechanisms (trap-coalesce-split) involved in it. Playback speed is 3.33x and 28x slower than realtime for the first part (trapping, coalescence, plug growth phase) and the second part (trapping, coalescence, splitting, stable plug phase) of the video, respectively.

**Movie S3:** Video showing the variation of generated drop characteristics - size and frequency with varying actuation voltage/ power by keeping other parameters unchanged. Playback speed is 13.33x slower than realtime.

**Movie S4:** Video showing the variation of generated drop characteristics - size and frequency with varying continuous phase flow rate by keeping other parameters unchanged. Three sub-videos are played sequentially at speeds 19x, 13.33x, and 13.33x slower than realtime, respectively.

**Movie S5:** Video showing the polydispersity in the incoming drops and improvement in drop homogeneity using ultrasound. Playback speed is 10x slower than realtime.

**Movie S6:** First part of the video showing the acoustic streaming inside the trapped plug, its variation with the acoustic power ramp up, and its role in setting up mixing inside the plug. Playback speed is 4x slower than realtime. Second part of the video showing vigorous Acousto-micromixing (attributed to acoustic streaming inside the trapped plug and acousto-coalescence of incoming drops with the trapped plug) inside the trapped plug while experiencing continuous drop coalescence and drop generation. Playback speed is 6.66x slower than realtime.

**Movie S7:** Video showing mixing of differently colored droplet with the plug inside the chamber due to the Acousto-micromixing. Playback speed is 67x slower than realtime.

- 
- 
- [1] L. Malik, A. Nath, S. Nandy, T. Laurell, and A. K. Sen, Acoustic particle trapping driven by axial primary radiation force in shaped traps, *Physical Review E* **105**, 1 (2022).
  - [2] H. Bruus, Acoustofluidics 7: The acoustic radiation force on small particles, *Lab on a Chip* **12**, 1014 (2012).
  - [3] L. D. Landau and E. M. Lifshitz, *Fluid Mechanics, Second Edition: Volume 6 (Course of Theoretical Physics)* (Butterworth-Heinemann, 1987).
  - [4] R. Barnkob, P. Augustsson, T. Laurell, and H. Bruus, Measuring the local pressure amplitude in microchannel acoustophoresis, *Lab on a Chip* **10**, 563 (2010).
  - [5] P. B. Muller, R. Barnkob, M. J. H. Jensen, and H. Bruus, A numerical study of microparticle acoustophoresis driven by acoustic radiation forces and streaming-induced drag forces, *Lab on a Chip* **12**, 4617 (2012).
  - [6] J. Lei, P. Glynne-Jones, and M. Hill, Acoustic streaming in the transducer plane in ultrasonic particle manipulation devices, *Lab on a Chip* **13**, 2133 (2013).
  - [7] P. Hahn, I. Leibacher, T. Baasch, and J. Dual, Numerical simulation of acoustofluidic manipulation by radiation forces and acoustic streaming for complex particles, *Lab on a Chip* **15**, 4302–4313 (2015).